

Dislocation injection in strontium titanate by femtosecond laser pulses

Michael S. Titus, McLean P. Echlin, Peter Gumbsch, and Tresa M. Pollock

Citation: *Journal of Applied Physics* **118**, 075901 (2015); doi: 10.1063/1.4928772

View online: <http://dx.doi.org/10.1063/1.4928772>

View Table of Contents: <http://scitation.aip.org/content/aip/journal/jap/118/7?ver=pdfcov>

Published by the [AIP Publishing](#)

Articles you may be interested in

[Electron backscatter diffraction on femtosecond laser sulfur hyperdoped silicon](#)

Appl. Phys. Lett. **101**, 111911 (2012); 10.1063/1.4752454

[Ablation and cutting of silicon wafer and micro-mold fabrication using femtosecond laser pulses](#)

J. Laser Appl. **19**, 240 (2007); 10.2351/1.2795754

[Microstructuring using femtosecond pulsed laser ablation](#)

J. Laser Appl. **18**, 227 (2006); 10.2351/1.2227020

[Efficiency of silicon micromachining by femtosecond laser pulses in ambient air](#)

J. Appl. Phys. **99**, 083101 (2006); 10.1063/1.2187196

[Comparison of heat-affected zones due to nanosecond and femtosecond laser pulses using transmission electronic microscopy](#)

Appl. Phys. Lett. **80**, 3886 (2002); 10.1063/1.1481195

The logo for AIP APL Photonics is displayed. It features the letters 'AIP' in a large, white, sans-serif font on the left, followed by a vertical line and the words 'APL Photonics' in a smaller, white, sans-serif font on the right. The background is a dark red with a bright yellow sunburst effect in the upper right corner.

APL Photonics is pleased to announce
Benjamin Eggleton as its Editor-in-Chief



Dislocation injection in strontium titanate by femtosecond laser pulses

Michael S. Titus,^{1,a)} McLean P. Echlin,^{1,b)} Peter Gumbsch,^{2,3} and Tresa M. Pollock¹

¹Materials Department, University of California Santa Barbara, Santa Barbara, California 93106-5050, USA

²Institute of Applied Materials (IAM), Karlsruhe Institute of Technology, Germany

³Fraunhofer IWM, Freiburg 79108, Germany

(Received 14 January 2015; accepted 6 August 2015; published online 19 August 2015)

Femtosecond laser ablation is used in applications which require low damage surface treatments, such as serial sectioning, spectroscopy, and micromachining. However, dislocations are generated by femtosecond laser-induced shockwaves and consequently have been studied in strontium titanate (STO) using transmission electron microscopy (TEM) and electron backscatter diffraction analysis. The laser ablated surfaces in STO exhibit dislocation structures that are indicative of those produced by uniaxial compressive loading. TEM analyses of dislocations present just below the ablated surface confirm the presence of $\langle 110 \rangle$ dislocations that are of approximately 35° mixed character. The penetration depth of the dislocations varied with grain orientation relative to the surface normal, with a maximum depth of $1.5 \mu\text{m}$. Based on the critical resolved shear stress of STO crystals, the approximate shockwave pressures experienced beneath the laser irradiated surface are reported. © 2015 AIP Publishing LLC. [<http://dx.doi.org/10.1063/1.4928772>]

I. INTRODUCTION

Perovskite oxides are frequently used as substrate materials for heterostructures and superconductors that require a room temperature cubic lattice, for high-voltage capacitors, and other electronic devices (e.g., piezoelectrics, varistors, ferroelectrics). Strontium titanate (STO) also has a wide range of cubic phase stability between -168°C and 1440°C , making it suitable for epitaxial growth across a wide range of temperatures. Previous work has shown that dislocations may be introduced by simple mechanical preparation techniques.¹ New low damage ultrashort pulsed lasers are promising tools for surface tailoring and the micromachining of materials that are highly prone to damage, or whose performance is degraded by the presence of dislocations, which are introduced during conventional processing approaches.^{2–6} With mJ pulse energies focused to μm -scale spots, a broad range of high strength materials,^{7,8} including composites⁹ and ceramics,¹⁰ may be ablated locally with kHz repetition rate pulses by a low-damage process.

The mechanisms for ablation are complex and vary depending on the properties of the material being irradiated and the laser beam parameters (e.g., beam fluence and profile). Femtosecond laser ablation experiments on dielectric materials have shown that material is ejected via a wide range of mechanisms,¹¹ which can be summarized as thermal and electrostatic in nature.¹² In the process of ejecting material from the surface, compressive and reflected tensile shockwaves are generated that propagate into the material below the ablated surface, as measured and simulated in semiconductors,¹³ metals,^{14,15} and dielectrics.^{16–18}

In the near-threshold ablation regime, which for STO (Ref. 19) starts above 1.2 J/cm^2 , the major form of damage observed following ablation involves the formation of

dislocation substructures immediately beneath the pulsed region. During irradiation by a femtosecond pulse (typically 150 fs for a Ti:Sapphire laser), the photon energy is absorbed by the electronic structure to 20–500 nm within the sample surface.^{20–23} The excited electron energy is then deposited after a time period of the order of 10 ps, during a thermalization event. Volumetric expansion of the highly excited surface region projects two waves: one compressive and, picoseconds later, a tensile wave that is reflected off the top surface of the expanding surface layer.^{15,21} These shockwaves result in glide of dislocations generated near the ablation events. One aim of this paper is to provide a detailed dislocation analysis that bounds the magnitude of the shockwaves necessary to generate and subsequently glide these defects.

II. METHODS

A polycrystalline STO sample surface was irradiated with a scanned femtosecond laser beam, ablating the surface region of a $300 \mu\text{m}$ diameter pillar-shaped sample with a laser fluence at the ablation threshold for STO, which is 1.2 J/cm^2 . This process is shown schematically in Figure 1(a).^{9,20} The stage on which the sample is mounted is composed of piezoelectric driven actuators (X, Y, Z, tilt) with 50 nm resolution that permit material removal by incrementally moving the sample surface into the scanning beam path, which is described in more detail elsewhere.^{9,20} A Ti:sapphire gain medium femtosecond laser operating at 780 nm wavelength and 1 kHz repetition rate was used to ablate the sample surface in a FIB-SEM vacuum chamber at a pressure of 4×10^{-6} mbar. The femtosecond laser beam is tightly focused into a 20–40 μm diameter spot and a $2 \times$ Rayleigh length of 0.39 mm, which has a Gaussian profile with the tail of the distribution decaying along the Z-direction, into the material, as shown in the inset in Figure 1(c). The sample surface was raised into the tail of the Gaussian beam in $1 \mu\text{m}$

^{a)}Electronic mail: mtitus@engineering.ucsb.edu

^{b)}Electronic mail: mechlin@engineering.ucsb.edu

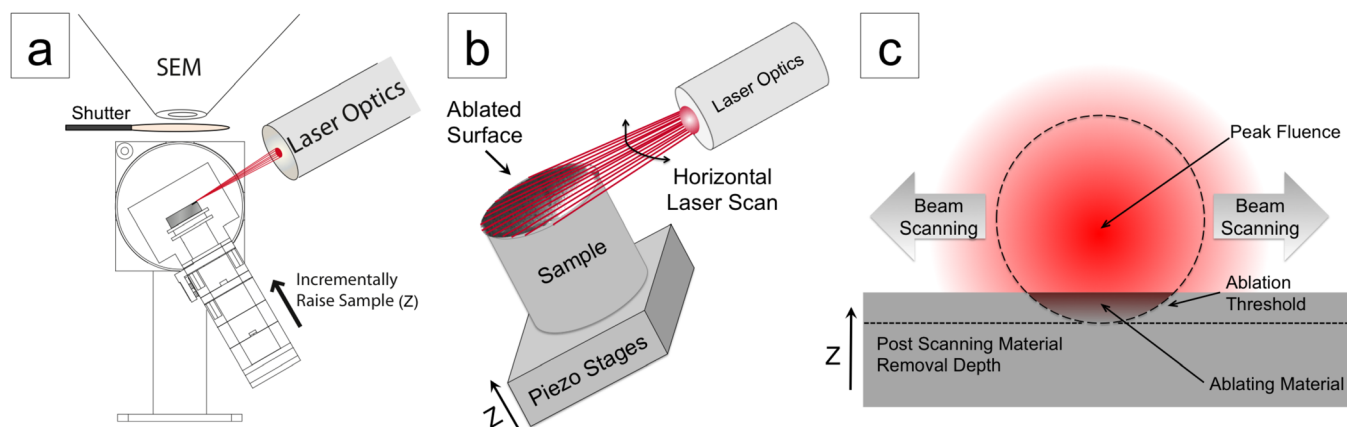


FIG. 1. (a) Schematic of the piezo positioner driven microstage in a modified scanning electron microscope with a focused ion beam (FIB-SEM) chamber which allows for *in-situ* femtosecond laser ablation using the TriBeam system.^{9,20} The sample is ablated such that the laser beam is orthogonal to the normal of the sample surface, with the beam propagation direction and scanning direction shown in (b). The beam is then scanned laterally across the sample surface, (c), with the peak fluence far above the sample surface. The radius of the beam, which is above the ablation threshold, removes sample material that is raised along the z-direction into the scanned beam via the piezoelectric actuators with 10 s of nm resolution.

increments using the Z-axis piezo actuator, after which the linearly S polarized laser beam was scanned horizontally across the sample surface with 75% pulse overlap in the scanning direction for 140 passes (roughly 10 000 pulses deposited on the pedestal), shown in Figure 1(c). Therefore, the freshly exposed laser cut surface, shown in Figure 2, is ultimately the product of the ablation generated right at the threshold value from the low-fluence tail of the Gaussian beam. The laser machining procedure used in this study is in contrast to other single pulse type laser machining studies or hole drilling, where the laser beam propagation direction is ortho-normal to the sample surface that experiences the full Gaussian distribution of the beam energy.

The transmission electron microscopy (TEM) lamellae were extracted from a sample that was sectioned in 1 μm increments to a depth of 100 μm during a 3-D electron backscatter diffraction (EBSD) tomography experiment, detailed elsewhere.²⁴ EBSD maps were collected from the laser machined lift-out areas using a FEI Quanta 3D FIB-SEM equipped with an EDAX Hikari XP EBSD in order to determine the grain orientations and Schmid factors of the grains contained in the TEM foils. Grain orientation information was collected with a 0.5 μm resolution at 70° tilt relative to the 25 keV electron beam operating at a 3 nA beam current. The pattern quality of EBSD maps did not vary between sections or with sectioning depth, indicating that there was no cumulative dislocation damage with progressive sections.

In order to investigate the damage imparted by the femtosecond laser, TEM analysis was carried out for STO grains that were oriented with their crystallographic normals of [100] and [110] parallel to the ablation surface normal. A TEM specimen was extracted from the pillar using a FEI dual-beam Helios Nanolab 600 FIB-SEM equipped with a W Omniprobe needle for lamella extraction. In order to ensure that ion damage or implantation did not occur on the specimen surface, the TEM lamella was protected with 500 nm of electron beam deposited Pt, followed by an additional 1.5 μm of ion-beam deposited Pt. The TEM lamella was investigated using a FEI T20 TEM operated at 200 keV in

both conventional bright-field and dark-field imaging modes. The dislocation characters were identified using conventional $\mathbf{g} \cdot \mathbf{b}$ analysis. Measurements of the penetration depths of dislocations and localized dislocation surface structures provided further insight into the plastic deformation mechanisms resulting from femtosecond laser ablation.

III. RESULTS

The region surrounding the TEM lamella was characterized using EBSD to provide local grain orientation information. The EBSD data are presented as an inverse pole figure (IPF) map with the out of plane normal used as the reference direction, as shown in Figure 3(a). The TEM liftout region is schematically indicated with a black box bisected by a line (the long axis of the foil). The sample foil spans two grains: one close to [110] orientation and the other close to [100] orientation (parallel to the surface normal). The actual grain orientations were determined to be [13 16 2] and [13 2 3], 8.1° and 15.5° away from the [110]- and [100]-grain orientations, respectively.

In the following analysis, it is assumed that the shock wave from the femtosecond laser pulse is predominantly of uniaxial compressive character and the direction of the uniaxial compression pulse entering from the surface is taken as the surface normal direction of a particular grain. The Schmid factor, which maps an applied uniaxial stress to the stress imparted on a dislocation, is calculated by

$$M = \cos(\phi) \cos(\lambda), \quad (1)$$

where ϕ is the angle between the direction of the uniaxial compression pulse entering from the surface and the Burgers vector, and λ is the angle between the direction of the uniaxial compression pulse entering from the surface and the slip plane normal. The Schmid factors were calculated assuming that slip primarily occurred on the $\langle 110 \rangle \{1\bar{1}0\}$ slip system, where $\langle \rangle$ and $\{ \}$ represent the dislocation Burgers vector (glide direction) and slip plane normal direction, respectively. A larger Schmid factor, M , indicates that a larger

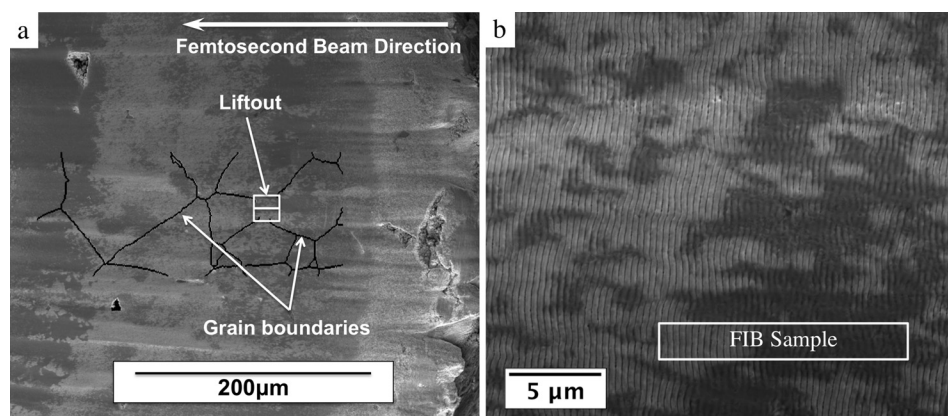


FIG. 2. The SEM images in parts (a) and (b) show the STO sample surface following laser ablation. (a) Also shows the grain boundaries, determined by EBSD, overlaid on the SEM micrograph as well as the TEM lamella liftout location and the propagation direction of the femtosecond laser beam. The FIB sample liftout location is shown in (b), and the laser-induced periodic surface structures (LIPSS) can be observed, which are typical of ultra-short pulse laser machining.^{25,26}

stress is resolved on a given slip system. As the resolved stresses exceed the critical resolved shear stress for dislocation motion, τ_{CRSS} , dislocations can glide into the depth of the material.

The largest Schmid factors for the $\langle 110 \rangle \{1\bar{1}0\}$ slip systems were determined to be 0.45 and 0.25 for the [100]-oriented and [110]-oriented grains, respectively, as shown in Figure 3(b). These slip systems were chosen based on previous research,^{27–30} which showed that the dislocations of $\langle 110 \rangle \{1\bar{1}0\}$ -type were commonly observed in uniaxial compression tests along the [100] and [110] directions over a large range of temperature (78–1800 K), as shown in Figure 3(c). In order to investigate the plastic deformation accrued and verify the presence of $\langle 110 \rangle \{1\bar{1}0\}$ -type dislocations created by the laser pulses, TEM analysis of the two grains was performed.

A composite TEM image of the FIB lamella is shown in Figure 4. The [110]-oriented grain (IPF: green colored) in Figure 3(a) corresponds to the grain in the left half of Figure 4. The femtosecond laser irradiated surface exhibits laser induced periodic surface structures (LIPSS), which are characteristic of repeatedly pulsed femtosecond laser ablated materials.^{25,26} These LIPSS structures are predominately observed in the [110]-oriented grain, indicated in Figure 4. The surface structures have a wavelength ranging from 350–450 nm, with crest to trough heights of about 100–200 nm, as measured from both TEM foil samples and from SEM images of the laser ablated surface. Along the surface and in the troughs of the LIPSS, no apparent recrystallization or amorphization was observed via selected area diffraction pattern analyses.

Elevated dislocation densities are observed within the first 100 nm of the ablated surface within both grains, with the highest densities visible in Figure 4 near the LIPSS troughs in the [110]-oriented grain. Notably, the [110]-oriented grain in Figure 4 is free of dislocations at depths greater than 100–200 nm from the surface, despite the [100]-oriented grain on the right exhibiting dislocations extending up to 1.5 μm into the bulk. Both grains were exposed to the same laser processing conditions, including number of laser pulses and laser fluence. Furthermore, the dislocation density consistently decreases with increasing depth from the laser irradiated surface, particularly when compared to the density near the LIPSS at the surface.

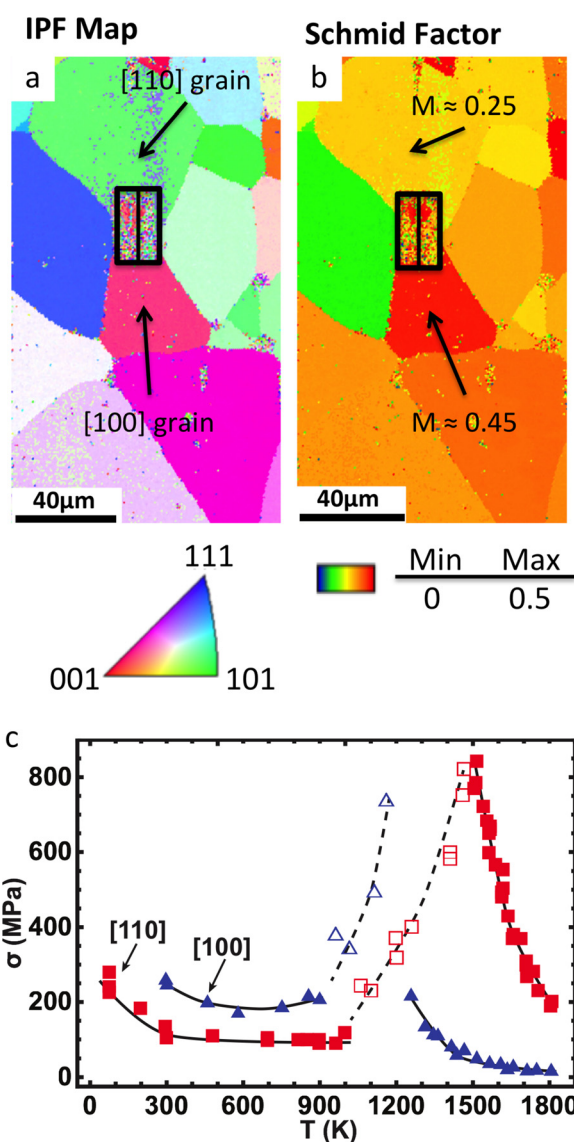


FIG. 3. Electron backscatter diffraction (EBSD) data were collected from the regions surrounding TEM lamella liftout locations to determine the grain orientations, shown in an inverse pole figure (IPF) map in (a) with the grain orientations indicated for two grains of interest. Part (b) is a Schmid factor map for the same region of interest shown in (a), calculated for primary slip on the $\langle 110 \rangle \{1\bar{1}0\}$. The plot in part (c), adapted from Gumbsch *et al.*,²⁷ shows the temperature dependence of single crystal compressive strength for STO crystal orientations of [100] and [110].

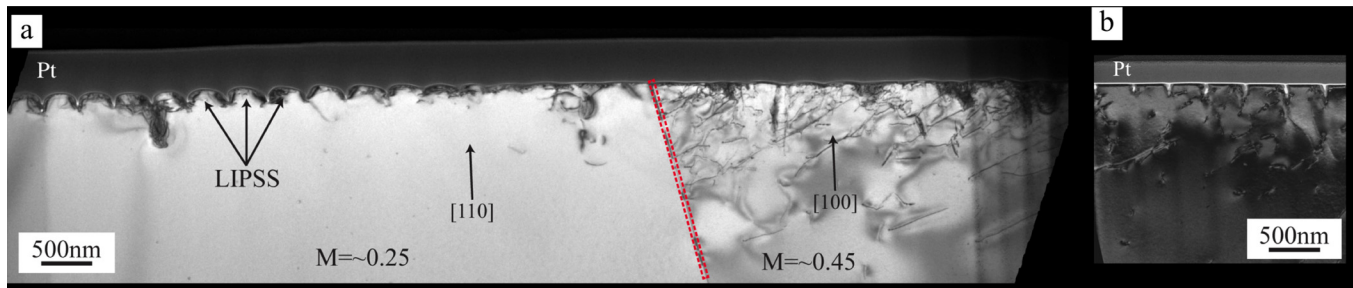


FIG. 4. (a) A composite TEM image of the STO FIB lamella shown in Figures 2 and 3. A grain boundary (dashed red box) divides the [110]-oriented grain (left region of the lamella) from the [100]-oriented grain. Numerous dislocations are observed greater than 800 nm from the surface in the [100]-oriented grain, but only a few spurious dislocations are observed beyond 100 nm from the surface in the [110]-oriented grain. The [110]- and [100]-oriented grains are colored green and red, respectively, in the IPF plot in Figure 3(a). The Schmid factors are labeled for each of the grain orientations (M). The TEM image in (b) shows the removal of near surface dislocations using near glancing angle FIB milling. Dislocations are observed far below the surface due to the soft [100]-orientation of the grain in (b).

A. Dislocation analysis

Conventional dislocation analysis was conducted to determine the character of the deeply-penetrating dislocations in the [100]-oriented grain. Three dislocation slip systems were characterized in the [100]-oriented grain and they are partially labeled in Figure 5(a) as 1, 2, and 3. Slip system 1 additionally includes all dislocations that exhibit double image contrast in Figure 5(a). Partial invisibility was observed for slip system 1 under $s=0$ conditions for $\mathbf{g} = [\bar{1}\bar{1}\bar{1}]$ and [110] reflections, as shown in Figures 5(b) and 5(c), respectively. Assuming that the Burgers vector, \mathbf{b} , is equal to a full unit cell translation vector (e.g., $a\langle 110 \rangle$, $a\langle 100 \rangle$, or $a\langle 111 \rangle$), the Burgers vector was determined to be $\mathbf{b} = [1\bar{1}0]$ for slip system 1.

The line directions for slip system 1 were determined using standard trace analyses, as explained elsewhere.³¹ The Burgers vector and line directions for slip system 1 are shown as red dots on the stereographic projection in Figure 6, where ζ indicates the line direction. Two different line directions were determined for slip system 1: $\zeta_1 = \sim [1\bar{1}\bar{1}]$ and $\sim [1\bar{1}1]$. The line directions are assumed to be near parallel to these directions, as these types of dislocations have been observed in previous investigations.¹ These line directions correspond to roughly 35° mixed dislocation character. The slip plane for slip system 1 was determined to be $(\bar{1}\bar{1}0)$, and thus the slip

system is $[1\bar{1}0](\bar{1}\bar{1}0)$. This slip system has a Schmid factor of 0.45, which matches the Schmid factor calculated via EBSD in Figure 3(b).

The dislocation characters of slip systems 2 and 3 were determined by the TEM analysis. Slip system 2 was determined to be of type $[\bar{1}01](101)$ and the dislocation character was similarly determined to be about 35° mixed with $\zeta_2 = [\bar{1}\bar{1}1]$, as shown in Figure 6. The Schmid factor for slip system 2 was calculated to be 0.44. Interestingly, slip system 3 was determined to be of type $[0\bar{1}1](0\bar{1}\bar{1})$, and the dislocation character was pure edge with $\zeta_3 = [\bar{1}00]$, as shown in Figure 6. The Schmid factor for this slip system is close to zero (0.01). Assuming a uniaxial stress state normal to the surface and therefore parallel to the $[1323]$ direction, a very low resolved shear stress is calculated for slip system 3. A summary of the three slip systems identified and their respective Schmid factors are given in Table I.

The dislocations within the first 100 nm of the surface in the [110]-oriented grain could not be identified due to the high dislocation density present. Four $\langle 110 \rangle\{1\bar{1}0\}$ slip systems possess Schmid factors approximately equal to 0.25 (systems 2 and 3), but tilting and diffraction contrast experiments were unable to identify slip planes or dislocation invisibility criteria. This indicates that multiple slip systems are present in the high dislocation density regions. However,

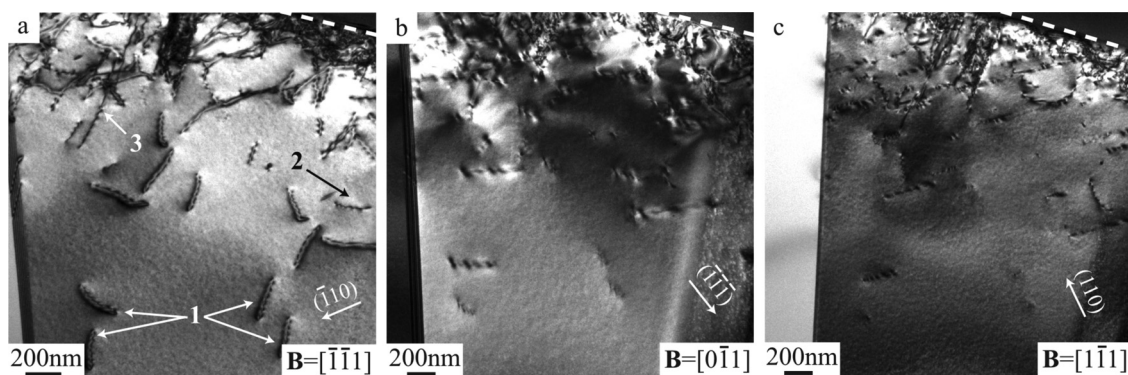


FIG. 5. Three dislocation slip systems are shown in the TEM micrographs (labeled 1, 2, 3) for the [100] oriented grain. All images were taken under $s=0$ conditions for various beam directions, shown in the bottom right of each figure. The double image contrast for slip system 1 dislocations suggests that $\mathbf{g} \cdot \mathbf{b} = 2$. Partial invisibility for slip system 1 dislocations is shown in (b) and (c). From these and other images not shown, the slip systems were determined to be 1— $\bar{1}\bar{1}0$; 2— $[\bar{1}01](101)$; 3— $[0\bar{1}1](0\bar{1}\bar{1})$. The dotted white lines in the upper right corners of (a)–(c) indicate the locations of the laser ablated surface with respect to the lamella.

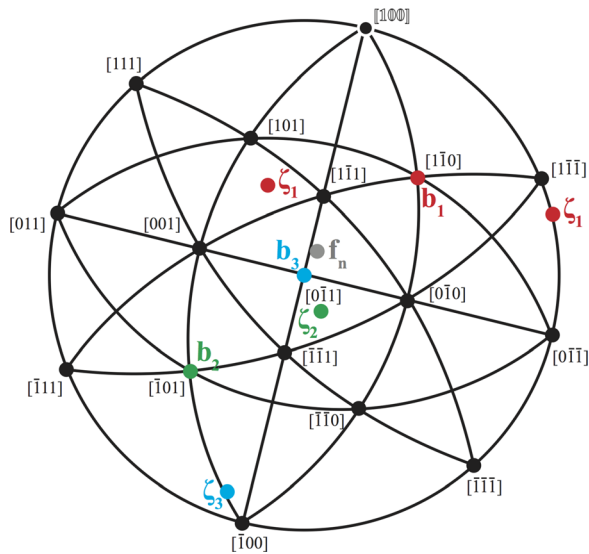


FIG. 6. The stereographic projection of the line directions (ζ), Burgers vectors (b), and the foil normal (f_n) is shown for all three characterized dislocation slip systems (1, 2, and 3) in the [100]-oriented grain, viewed from approximately the $[01 \bar{1}]$ direction.

the high density of dislocations within the first 100 nm of the surface is easily removed by near glancing angle FIB milling,²⁴ as shown in the TEM micrographs in Figure 4(b).

B. Dislocation penetration depths

Dislocations that penetrated to the greatest extent in the [100]-oriented grain also possessed the largest resolved shear stress and Schmid factor. The stresses required to enable glide of $\langle 110 \rangle \{ \bar{1}10 \}$ dislocations to depths greater than 800 nm must exceed the critical resolved shear stress (τ_{CRSS}). In works by Brunner *et al.*²⁹ and Gumbsch *et al.*,²⁷ the flow stress for compressively loaded single crystals of STO was measured for both the [110]- and [100]-oriented crystals, across a range of temperature, as shown in the plot reproduced in Figure 3(c). These measurements indicate that

TABLE I. The Schmid factor, critical resolved stress (σ_c), and max depth at which dislocations of slip systems 1, 2, and 3 were found from the TEM analysis are shown here. Note that dislocations from system 1 are pushed the deepest into the material by the laser ablation shockwaves generated as the pulsed beam was rastered over the surface. Very few dislocations were observed deeper than 50–150 nm from the surface in the [110]-oriented grain.

[100]-oriented grain			
	System 1 $\bar{1}\bar{1}0$	System 2 $[\bar{1}01](101)$	System 3 $[0\bar{1}1](0\bar{1}\bar{1})$
Schmid factor	0.45	0.44	0.01
σ_c (MPa)	140	140	6000
Maximum depth (μm)	1.5	0.8	0.7
[110]-oriented grain			
	System 1 $\bar{1}\bar{1}0$	System 2 $[\bar{1}01](101)$	System 3 $[0\bar{1}1](0\bar{1}\bar{1})$
Schmid factor	0.10	-0.19	0.29
σ_c (MPa)	600	320	210
Maximum depth (μm)	0.1	0.1	0.1

[110]- and [100]-oriented crystals exhibit flow stresses of 120 MPa and 250 MPa, respectively, for the temperature range between 300 and 900 K, as shown in Figure 3(c), which translates into a τ_{CRSS} of 60–70 MPa, assuming glide on the 110 slip system. These calculations do assume that the temperature of material where dislocation is gliding remains within 300–900 K. Temperature profile estimates from molecular dynamics simulations in metallic systems,¹⁵ which have much higher thermal conductivities than dielectrics, provide an upper bound on heating due to femtosecond laser ablation. At depths greater than 100 nm below the ablated surface for gold targets, the temperature profile remains below 1000 K. Therefore, the high temperatures experienced during femtosecond laser irradiation are confined to the ejected liquid-like layer in the ablating material and the very near subsurface in metals and dielectric materials, particularly at ablation threshold.

The critical uniaxial stress, σ_c , required to glide dislocations with an applied stress parallel to the $[1323]$ direction can be determined by

$$\sigma_c = \tau_{CRSS}/M. \quad (2)$$

The critical uniaxial stresses required for glide are given for the three observed slip systems in Table I. This analysis indicates that a relatively modest uniaxial stress (~ 140 MPa) enables dislocation glide for slip systems exhibiting Schmid factors near 0.45. However, for the case of slip system 3, a uniaxial stress of 6 GPa would be needed for dislocation glide.

IV. DISCUSSION

Femtosecond laser-material interactions are fundamentally complex to model because of the disparate temporal length scales at which material response occurs (nanoseconds) compared with the equilibration of the energy absorbed via photons (femtoseconds to picoseconds). Furthermore, the volume of material that has been highly excited via photon absorption and electron diffusion often undergoes a phase transformation and fast volumetric expansion, dynamically modifying the local material properties and generating GPa-scale shockwaves which may propagate back through the ejecting material and into the depth of the sample bulk. Therefore, experimental measurements of ablation dynamics, such as the shockwaves generated due to ablation,¹⁴ the velocity of ablated material,^{32,33} and the mechanisms for formation of laser induced surface structuring (e.g., LIPSS),^{34,35} are of great value for validation of models for the ablation process.

Analysis of the dislocations injected into the [100]-oriented STO grain subjected to a laser ablation event has revealed a tendency for dislocation nucleation near the ablated surface which likely serves to relax stresses imparted by the laser ablation event. Previous molecular dynamics simulations^{14,15} and *in-situ* diffraction experiments^{36,37} have indicated that GPa-scale stress waves, first compressive and then tensile, propagate into the depth below the ablated surface in the timeframe of hundreds of picoseconds after laser irradiation. The stresses near the ablating surface are

initially very high, but decay quickly as the stress wave moves into the bulk. In regions deeper than the initial 100–200 nm, glide of dislocations occurs in instances where the critical resolved shear stresses for dislocation glide are relatively low. The rates at which the dislocations glide in this experiment are unknown and may be higher than employed in the measurements²⁷ shown in Figure 3(c); for this reason, the stresses estimated from the present experiment represent an upper bound.

For materials with strong covalent bonding, it would thus be expected that material removal could be accomplished with very limited dislocation injection. As such, dislocations should be present near the surface in all STO grains at the laser ablation conditions used during this experiment. Indeed, for the differently oriented grains investigated here, numerous dislocations were always present within the first 100 nm of the surface. These dislocations can be removed by near glancing angle FIB milling to remove the surface layer of the laser machined surface, as shown in Figure 4(b).

Due to the nucleation of a high density of dislocations, the high incidence of dislocation-dislocation interactions within the first 100 nm from the ablated surface in this experiment will govern the final structure in that region. As such, dislocations may become pinned by the presence of other dislocations, and may not be able to glide deeper into the material even after multiple laser pulses. This is evidenced by the high near-surface dislocation density in the [110]-oriented grain, as shown in Figure 4, where the near-surface dislocations in the [110]-oriented grain likely belonged to many different slip systems as neither complete invisibility nor edge-on slip plane configurations were obtained.

The critical uniaxial stresses required for shearing in the [110]-oriented grain range from 210 to 600 MPa (due to the differing orientations of the potential slip systems). Because dislocations were not observed greater than about 100 nm from the ablation surface in the [110]-oriented grain, conclusions may not be drawn regarding the magnitude of the stresses present due to the multi-slip configuration and the very similar Schmid factors on different dislocations.

In a few instances, dislocations with low resolved shear stress were observed at depths greater than 100 nm, as for example, the dislocations of slip system 3 in Figure 5. The critical uniaxial stress, σ_c , required for dislocation glide on this slip system in the [100]-oriented grain was determined to be 6 GPa (Table I). However, these dislocations could be a product of dislocation reactions at this depth or may have also been pre-existing prior to laser ablation.

Dislocation glide to distances deeper than 700 nm from the surface appears to be possible for dislocations on systems with large Schmid factors, assuming the correct type of dislocation is nucleated during the ablation process and that dislocation-dislocation interactions do not impede dislocation motion. A dislocation that glides a distance of 1 μm in 100 ps would possess a glide velocity of the order of 10^4 m/s, as an upper limit, considering that it may glide under the action of multiple pulses. This is about the same order of magnitude of the acoustic wave velocity in STO.³⁸

The presence of both dislocations with high resolved shear stresses (e.g., [110](1 $\bar{1}$ 0)) deep in the material and

dislocations with low resolved shear stress (e.g., [0 $\bar{1}$ 1](0 $\bar{1}$ $\bar{1}$)) closer to the ablated surface in the [100]-oriented grain indicates that the stress wave decays rapidly within the first 800 nm of the ablated surface. This implies that stresses are large enough near the surface to generate almost all types of dislocations. However, only well-oriented, glissile dislocations may then glide to greater depths (of the order of a micron) where stresses appear to be much lower.

Multiple laser pulses per position and dislocation-dislocation repulsive and attractive forces all make for significant conclusions to be drawn from depths less than about 800 nm from the surface. However, the uniaxial stress present at depths between 0.8 μm and 1.5 μm may be concluded to be certainly above 140 MPa, and likely no more than about 210 MPa.

In addition to the shockwaves present during the ablation event, extreme temperature excursions affecting the first 100 nm of material provide conditions suitable for nucleation of dislocations. Thus, the presence of dislocations in the material at depths of micrometers and greater is present due to glide from the surface and is strongly influenced both by the decay of the compressive wave and the magnitude of the critical resolved shear stress on the relevant slip planes. For materials, such as STO, that have a high degree of plastic anisotropy, laser-induced dislocation damage is expected to vary on a grain-by-grain basis. Conversely, for materials exhibiting less plastic anisotropy, damage would be expected to be much more homogeneous because the critical resolved shear stresses would not vary as strongly from grain to grain. The magnitude and extent of the temperature profile immediately below the surface will vary with materials and experimental conditions,^{6,8,39–41} including laser ablation fluence, sample thickness, and orientation of laser beam to the sample surface.

V. CONCLUSION

In summary, the following conclusions can be made about damage adjacent to the femtosecond laser ablated surfaces in STO:

1. The vast majority of dislocations induced by femtosecond laser machining are located within 100–150 nm of the surface. These are easily removed with a near glancing angle FIB milling operation.
2. Dislocations of type $\langle 110 \rangle \{ \bar{1}\bar{1}0 \}$ with large Schmid factors (>0.4) were observed at depths between 0.8 and 1.5 μm , at significantly lower densities than the surface dislocation structure.
3. The dislocations which were subject to glide over the largest distances into the sample were found to be of approximately 35° mixed character.
4. Based on the critical resolved shear stresses for glide, stresses at depths greater than about 800 nm were limited to 140–210 MPa as a result of the dynamics of the ablation event.

ACKNOWLEDGMENTS

This research was supported by AFRL Center of Excellence Grant No. FA9550-12-1-0445, ONR Grant Nos.

(N00014-14-1-0618, and N00014-10-10783), and the MRL Shared Experimental Facilities are supported by the MRSEC Program of the NSF under Award No. DMR 1121053; a member of the NSF-funded Materials Research Facilities Network (www.mrfn.org). We thank Michael Uchic (Air Force Research Labs) and Marc De Graef (Carnegie Mellon University) for useful discussion on instrumentation and Marcus Straw (FEI Company) for discussion on femtosecond laser-induced damage.

- ¹L. Jin, X. Guo, and C. L. Jia, "Tem study of $\langle 110 \rangle$ -type 35.26° dislocations specially induced by polishing of srtio3 single crystals," *65th Birthdays of W Owen Saxton, David J Smith and Dirk Van Dyck / PICO 2013 & From Multislice to Big Bang*, *Ultramicroscopy* **134**, 77–85 (2013).
- ²A. Borowiec, M. MacKenzie, G. Weatherly, and H. Haugen, "Transmission and scanning electron microscopy studies of single femtosecond-laser-pulse ablation of silicon," *Appl. Phys. A: Mater. Sci. Process.* **76**, 201–207 (2003).
- ³E. Coyne, J. Magee, P. Mannion, G. O'Connor, and T. Glynn, "Stem (scanning transmission electron microscopy) analysis of femtosecond laser pulse induced damage to bulk silicon," *Appl. Phys. A: Mater. Sci. Process.* **81**, 371–378 (2005).
- ⁴A. Kumar and T. Pollock, "Mapping of femtosecond laser-induced collateral damage by electron backscatter diffraction," *J. Appl. Phys.* **110**, 083114 (2011).
- ⁵P. P. Pronko, S. K. Dutta, J. Squier, J. V. Rudd, D. Du, and G. Mourou, "Machining of sub-micron holes using a femtosecond laser at 800 nm," *Opt. Commun.* **114**, 106–110 (1995).
- ⁶Q. Feng, Y. Picard, H. Liu, S. Yalisove, G. Mourou, and T. Pollock, "Femtosecond laser micromachining of a single-crystal superalloy," *Scr. Mater.* **53**, 511–516 (2005).
- ⁷M. P. Echlin and T. M. Pollock, "A statistical sampling approach for measurement of fracture toughness parameters in a 4330 steel by 3-d femtosecond laser-based tomography," *Acta Mater.* **61**, 5791–5799 (2013).
- ⁸S. Ma, J. McDonald, B. Tryon, S. Yalisove, and T. Pollock, "Femtosecond laser ablation regimes in a single-crystal superalloy," *Metall. Mater. Trans. A* **38**, 2349–2357 (2007).
- ⁹M. P. Echlin, A. Mottura, M. Wang, P. J. Mignone, D. P. Riley, G. V. Franks, and T. M. Pollock, "Three-dimensional characterization of the permeability of w-cu composites using a new "tribeam" technique," *Acta Mater.* **64**, 307–315 (2014).
- ¹⁰D. K. Das, J. P. McDonald, C. G. Levi, S. M. Yalisove, and T. M. Pollock, "Detection of a marker layer in a 7ysz thermal barrier coating by femtosecond laser-induced breakdown spectroscopy," *Surf. Coat. Technol.* **202**, 3940–3946 (2008).
- ¹¹P. Balling and J. Schou, "Femtosecond-laser ablation dynamics of dielectrics: basics and applications for thin films," *Rep. Prog. Phys.* **76**, 036502 (2013).
- ¹²E. N. Glezer and E. Mazur, "Ultrafast-laser driven micro-explosions in transparent materials," *Appl. Phys. Lett.* **71**, 882–884 (1997).
- ¹³P. Lorazo, L. J. Lewis, and M. Meunier, "Short-pulse laser ablation of solids: From phase explosion to fragmentation," *Phys. Rev. Lett.* **91**, 225502 (2003).
- ¹⁴B. J. Demaske, V. V. Zhakhovskiy, N. A. Inogamov, and I. I. Oleynik, "Ablation and spallation of gold films irradiated by ultrashort laser pulses," *Phys. Rev. B* **82**, 064113 (2010).
- ¹⁵C. Wu, M. S. Christensen, J.-M. Savolainen, P. Balling, and L. V. Zhigilei, "Generation of subsurface voids and a nanocrystalline surface layer in femtosecond laser irradiation of a single-crystal Ag target," *Phys. Rev. B* **91**, 035413 (2015).
- ¹⁶A. Horn, E. Kreutz, and R. Poprawe, "Ultrafast time-resolved photography of femtosecond laser induced modifications in bk7 glass and fused silica," *Appl. Phys. A* **79**, 923–925 (2004).
- ¹⁷M. Sakakura, M. Terazima, Y. Shimotsuma, K. Miura, and K. Hirao, "Observation of pressure wave generated by focusing a femtosecond laser pulse inside a glass," *Opt. Express* **15**, 5674–5686 (2007).
- ¹⁸H. Hu, X. Wang, H. Zhai, N. Zhang, and P. Wang, "Generation of multiple stress waves in silica glass in high fluence femtosecond laser ablation," *Appl. Phys. Lett.* **97**, 061117 (2010).
- ¹⁹F. Watanabe, D. G. Cahill, B. Gundrum, and R. S. Averback, "Ablation of crystalline oxides by infrared femtosecond laser pulses," *J. Appl. Phys.* **100**, 083519 (2006).
- ²⁰M. P. Echlin, M. Straw, S. Randolph, J. Filevich, and T. M. Pollock, "The tribeam system: Femtosecond laser ablation in situ {SEM}," *Mater. Charact.* **100**, 1–12 (2015).
- ²¹B. Demaske, V. Zhakhovskiy, N. Inogamov, and I. Oleynik, "Ultrashort shock waves in nickel induced by femtosecond laser pulses," *Phys. Rev. B* **87**, 054109 (2013).
- ²²J. P. Colombier, P. Combis, F. Bonneau, R. Le Harzic, and E. Audouard, "Hydrodynamic simulations of metal ablation by femtosecond laser irradiation," *Phys. Rev. B* **71**, 165406 (2005).
- ²³B. Chichkov, C. Momma, S. Nolte, F. von Alvensleben, and A. Tünnermann, "Femtosecond, picosecond and nanosecond laser ablation of solids," *Appl. Phys. A* **63**, 109–115 (1996).
- ²⁴W. C. Lenthe, M. P. Echlin, A. Trenkle, M. Syha, P. Gumbsch, and T. M. Pollock, "Quantitative voxel-to-voxel comparison of TriBeam and DCT strontium titanate three-dimensional data sets," *J. Appl. Crystallogr.* **48**, 1034–1046 (2015).
- ²⁵J. Bonse, S. Baudach, J. Krüger, W. Kautek, and M. Lenzner, "Femtosecond laser ablation of silicon—modification thresholds and morphology," *Appl. Phys. A* **74**, 19–25 (2002).
- ²⁶J. Bonse and J. Krüger, "Pulse number dependence of laser-induced periodic surface structures for femtosecond laser irradiation of silicon," *J. Appl. Phys.* **108**, 034903 (2010).
- ²⁷P. Gumbsch, S. Taeri-Baghdarani, D. Brunner, W. Sigle, and M. Rühle, "Plasticity and an inverse brittle-to-ductile transition in strontium titanate," *Phys. Rev. Lett.* **87**, 085505 (2001).
- ²⁸S. Taeri, D. Brunner, W. Sigle, and M. Rühle, "Deformation behaviour of strontium titanate between room temperature and 1800 k under ambient pressure," *Z. Metall.* **95**, 433–446 (2004).
- ²⁹D. Brunner, S. Taeri-Baghdarani, W. Sigle, and M. Rühle, "Surprising results of a study on the plasticity in strontium titanate," *J. Am. Ceram. Soc.* **84**, 1161–1163 (2001).
- ³⁰D. Brunner, "Low-temperature plasticity and flow-stress behaviour of strontium titanate single crystals," *Acta Mater.* **54**, 4999–5011 (2006).
- ³¹J. Edington, *Practical Electron Microscopy in Materials Science* (Van Nostrand Reinhold Co., 1976).
- ³²X. Zeng, X. Mao, R. Greif, and R. Russo, "Experimental investigation of ablation efficiency and plasma expansion during femtosecond and nanosecond laser ablation of silicon," *Appl. Phys. A* **80**, 237–241 (2005).
- ³³J. P. McDonald, S. Ma, T. M. Pollock, S. M. Yalisove, and J. A. Nees, "Femtosecond pulsed laser ablation dynamics and ablation morphology of nickel based superalloy CMSX-4," *J. Appl. Phys.* **103**, 093111 (2008).
- ³⁴Z. Guosheng, P. Fauchet, and A. Siegman, "Growth of spontaneous periodic surface structures on solids during laser illumination," *Phys. Rev. B* **26**, 5366–5381 (1982).
- ³⁵M. Huang, F. Zhao, Y. Cheng, N. Xu, and Z. Xu, "Origin of laser-induced near-subwavelength ripples: Interference between surface plasmons and incident laser," *ACS Nano* **3**, 4062–4070 (2009).
- ³⁶C. W. Siders, A. Cavalleri, K. Sokolowski-Tinten, C. Tóth, T. Guo, M. Kammler, M. H. V. Hoegen, K. R. Wilson, D. V. D. Linde, and C. P. J. Barty, "Detection of nonthermal melting by ultrafast x-ray diffraction," *Science* **286**, 1340–1342 (1999).
- ³⁷K. Sokolowski-Tinten, C. Blome, C. Dietrich, A. Tarasevitch, M. Horn von Hoegen, D. von der Linde, A. Cavalleri, J. Squier, and M. Kammler, "Femtosecond x-ray measurement of ultrafast melting and large acoustic transients," *Phys. Rev. Lett.* **87**, 225701 (2001).
- ³⁸R. O. Bell and G. Rupprecht, "Elastic constants of strontium titanate," *Phys. Rev.* **129**, 90–94 (1963).
- ³⁹S. Nolte, C. Momma, H. Jacobs, A. Tünnermann, B. N. Chichkov, B. Wellegehausen, and H. Welling, "Ablation of metals by ultrashort laser pulses," *J. Opt. Soc. Am. B* **14**, 2716–2722 (1997).
- ⁴⁰Y. Hirayama and M. Obara, "Heat-affected zone and ablation rate of copper ablated with femtosecond laser," *J. Appl. Phys.* **97**, 064903 (2005).
- ⁴¹Y. N. Picard and S. M. Yalisove, "Femtosecond laser heat affected zones profiled in CoSi multilayer thin films," *Appl. Phys. Lett.* **92**, 014102 (2008).